Electrodeposited Defect Chemistry Superlattices

Jay A. Switzer,* Chen-Jen Hung, Bryan E. Breyfogle, Mark G. Shumsky, Robert Van Leeuwen, Teresa D. Golden

Nanometer-scale layered structures based on thallium(III) oxide were electrodeposited in a beaker at room temperature by pulsing the applied potential during deposition. The conducting metal oxide samples were superlattices, with layers as thin as 6.7 nanometers. The defect chemistry was a function of the applied overpotential: High overpotentials favored oxygen vacancies, whereas low overpotentials favored cation interstitials. The transition from one defect chemistry to another in this nonequilibrium process occurred in the same potential range (100 to 120 millivolts) in which the rate of the back electron transfer reaction became significant. The epitaxial structures have the high carrier density and low electronic dimensionality of high transition temperature superconductors.

Electrodeposition is unique among thin-film processing techniques because the driving force of the reaction is precisely known and controlled. We exploited the intimate interplay of kinetics and thermodynamics in electrochemistry to deposit superlattices based on thallium(III) oxide in which the defect chemistry is modulated on a nanometer scale. We define defect chemistry as charge compensation reactions that must occur in a nonstoichiometric material to preserve charge neutrality. For example, in an *n*-type material such as thallium(III) oxide in which the majority carriers are electrons, defect reactions such as the creation of oxygen vacancies, cation interstitials, or altervalent substitutions (substitution of an ion in a different oxidation state) ensure that the overall charge on the solid is zero.

The defect chemistry superlattices in our study are layered materials that have the high carrier density and low electronic dimensionality that are characteristic of high transition temperature (T_c) superconductors (*1*, *2*). One goal of our work is to produce an artificial superconductor by alternating nanometer-thick layers of high carrier concentration ("charge reservoir layers") with nanometer-thick layers of high carrier mobility. Laguës *et al.* have recently used sequentially imposed layer epitaxy to deposit an artificial cuprate of the BiSrCaCuO system with eight adjacent CuO_2 layers, which shows evidence of superconductivity at 250 K (*3*). Our focus is on materials that have no CuO_2 planes. A notable example of a noncuprate superconductor is $Ba_{1-x}K_xBiO_3$, which can be electrocrystallized as centimeter-scale single crystals (*4*–*7*).

The defect chemistry of nonstoichiometric oxides is usually controlled by annealing at high temperature in an atmosphere of known oxygen partial pressure and then quenching by rapid cooling of the sample. This type of treatment is used to control the stoichiometry of high T_c superconductors. The defect chemistry of oxides can also be controlled electrochemically (*8*–*10*). Grenier *et al.* have used electrochemical oxidation to intercalate oxygen into La_2CuO_4, producing a superconductor with a critical temperature of 50 K (*8*). This treatment, like high-temperature annealing, cannot be used to modulate the defect chemistry in the material.

We have previously shown that it is possible to grow nanometer-scale superlattices in the Pb-Tl-O system by modulating either the applied potential or current during the deposition (*11*, *12*). Superlattices with layers as thin as 3 nm were produced. This is a nonequilibrium process, and the overpotential, η, is a direct measure of departure from equilibrium ($\eta = E_{applied} - E_{equilibrium}$). We determined in previous work using scanning tunneling microscopy (STM) that the composition profile in Pb-Tl-O superlattices followed the applied potential more closely than it followed the applied current (*13*, *14*).

As a control experiment in this previous work, we examined cleaved cross sections of "pure" thallium(III) oxide films by STM (Fig. 1), which we grew by pulsing the overpotential between 90 and 300 mV (*15*). Layers corresponding to the calculated Faraday thicknesses are evident for these films, with the layer deposited at 300 mV having a higher apparent height than the layer grown at the lower overpotential. The quality of the STM images was a strong function of the cleavage process. Individual superlattice layers were typically discernible over a 1- to 2-μm scan width. This is the approximate width of the columnar grains in the electrodeposited films. The contrast in the STM image could be attributable to electronic differences between the layers or true physical corrugation caused either by elastic deformation driven by strain relief or by composition-dependent surface reactions (*13*, *16*, *17*). Regardless of the imaging mechanism, the STM experiments were important because they showed us that the thallium(III) oxide films were layered.

The thallium(III) oxide multilayers grown by potential pulsing are also superlattices, as shown by x-ray diffraction. The x-ray pattern of a sample that was grown with a modulation wavelength of 13.4 nm is shown in Fig. 2. Each layer in the superlattice is 6.7 nm thick. The sample is strongly oriented with the (100) planes parallel with the electrode surface. In addition, the Bragg peaks in the pattern are flanked by superlattice satellites. The satellites are caused by the superperiodicity in the system, because the x-ray pattern is the Fourier transform of the product of the lattice and modulation functions convoluted with the basis (*18*). The wavelength of this superperiodicity can be calculated from the satellite spacing (*11*). The intensities of the superlattice satellites are 2% of the Bragg peak, compared with 14% for the Pb-Tl-O compositional superlattices of the same modulation wavelength in our previous work.

The lattice parameter of bulk (that is, 10 μm thick) thallium(III) oxide films varies from 1.0518 nm at an overpotential of 44

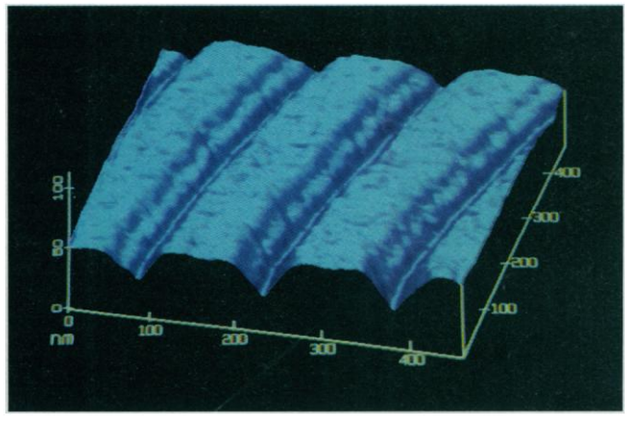

Fig. 1. An STM image of cleaved thallium(III) oxide defect chemistry superlattice deposited by pulsing the overpotential between 90 and 300 mV. The higher overpotential layer has a higher apparent height in the STM image.

Department of Chemistry and Graduate Center for Materials Research, University of Missouri–Rolla, Rolla, MO 65401, USA.

*To whom correspondence should be addressed.

mV to 1.0556 nm at 535 mV (Fig. 3A). The lattice mismatch for the layers of the electrodeposited superlattice is about 0.2%. The curve of lattice parameter versus overpotential resembles a titration curve, with the transition from one defect chemistry to another occurring between 100 and 150 mV. The films were also found by flame emission spectrometry to contain excess thallium. The excess thallium increased from 0.3 to 5 atomic percent as the potential was decreased from 535 to 44 mV, with the sharpest increase at overpotentials between 100 and 120 mV (Fig. 3A). These results are consistent with the electrochemical formation of thallium interstitials at potentials below about 120 mV.

To better understand the mechanism of the formation of thallium interstitials at low overpotential, we investigated the kinetics of the electrodeposition reaction by analysis of a Tafel plot of the log of the deposition current density (j) versus the applied overpotential (η) (*19*). The Tafel equation for an anodic reaction is

$$j = j_0 e^{\alpha n F \eta / RT} \quad (1)$$

where n is the number of electrons transferred in the rate-determining step, F is Faraday's number, R is the molar gas constant, T is the absolute temperature (F/RT = 38.92 V^{-1} at 298 K), α is the transfer coefficient (equal to 0.5 for a symmetrical energy barrier), j is the measured current density, and j_0 is the exchange current density. Linear Tafel behavior is usually observed in systems that are kinetically sluggish.

In a chemically reversible system, the exchange current density is the equilibrium current density of both the anodic (forward) and the cathodic (back) reactions. At zero overpotential, the system is at equilibrium and the anodic and cathodic components add to zero. As a positive overpotential is applied, the rate of the forward reaction increases exponentially, and the rate of the back reaction decreases exponentially. The linear Tafel region is the range of potentials at which the back reaction can be neglected. This transition occurs at 118 mV for a one-electron process with α = 0.5, because the rate of the back reaction is 1% of the rate of the forward reaction at that overpotential (*19*).

The Tafel plot (Fig. 3B) exhibits a linear dependence in the region from 102 to 308 mV. The Tafel slope is 110 ± 5 mV and the exchange current density is 1.9 (±0.7) × 10^{-5} A/cm^2. The Tafel slope indicates that the rate of the reaction increases 10-fold for every 110-mV change in overpotential. This is consistent with a reaction with one electron transferred in the rate-determining step and α = 0.54 ± 0.02. Deviation from ideal Tafel behavior occurs when the overpotential exceeds 308 ± 13 mV because of mass-transport effects and when the overpotential is less than 102 ± 11 mV as a result of the back reaction. The low overpotential deviation is particularly important for this study because it marks the potential at which partial reduction of the film occurs. There is good agreement between the potential at which the back reaction becomes important and when the excess thallium content of the film increases. We interpret this to indicate that a portion of the back-reaction current is reducing lattice thallium(III) to thallium(I) and driving the intercalation half-reaction

$$Tl_2O_3 + xe^- + xTl^+ = Tl_xTl_2O_3 \quad (2)$$

where x = 0.02 to 0.10.

The electrical properties of the films were also measured as a function of the deposition overpotential. The samples were found to be n-type degenerate semiconductors. They have a sharp plasma resonance at about 1300 nm in the near infrared owing to the high concentration of free electrons. The resistivity (Fig. 3C) rises at overpotentials below 100 to 120 mV, in good agreement with the increase in excess thallium content and the deviation from ideal Tafel behavior at the same range of overpotentials. Because the carrier density was nearly constant at about 5 × 10^{20} cm^{-3} throughout this range, the increase in resistivity is mainly the result of a decrease in electron mobility. The electron mobility decreased from 169 to 7 cm^2 V^{-1} s^{-1} as the overpotential was decreased from 535 to 44 mV (Fig. 3C). The decrease in mobility is consistent with an increase in concentration of charged interstitials.

If Eq. 2 were the only defect reaction producing free carriers, the carrier density would decrease at high overpotentials. Thallium(III) oxide has an optical band gap of 1.4 eV (*20*, *21*), and the intrinsic carrier density would be only about 10^6 cm^{-3}, rather than the observed 5 × 10^{20} cm^{-3}. We believe that the carriers in the films produced at high overpotential result from an internal redox reaction in which thallium(III) is reduced to thallium(I) and oxygen vacancies are produced. This would be represented as a chemical reaction by

$$Tl_2O_3 = Tl_2O_{3-x} + \frac{x}{2} O_2 \quad (3)$$

and in Kröger-Vink notation by (*22*)

$$O_O + Tl_{Tl} = V_O^{\cdot\cdot} + Tl''_{Tl} + \frac{1}{2} O_2 \quad (4)$$

The symbol Tl''_{Tl} designates that a lattice thallium(III) has been reduced to thallium(I), producing a site that has a double negative charge relative to its original charge. If the carriers are assumed to be "free" carriers and not localized on a particular site, the Kröger-Vink expression

$$O_O = V_O^{\cdot\cdot} + 2e' + \frac{1}{2} O_2 \quad (5)$$

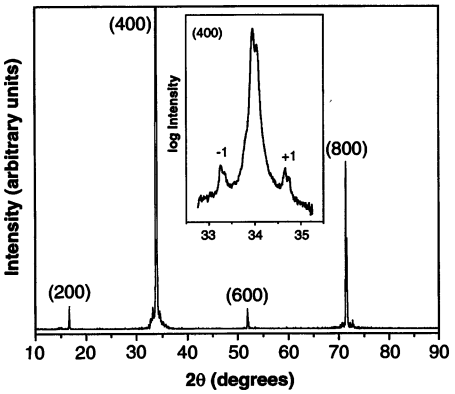

Fig. 2. The x-ray diffraction pattern of a [100]-textured superlattice produced under potential control. The modulation wavelength (that is, the sum of the bilayer thicknesses) calculated from the satellite spacing is 13.4 nm. The x-ray radiation is CuKα.

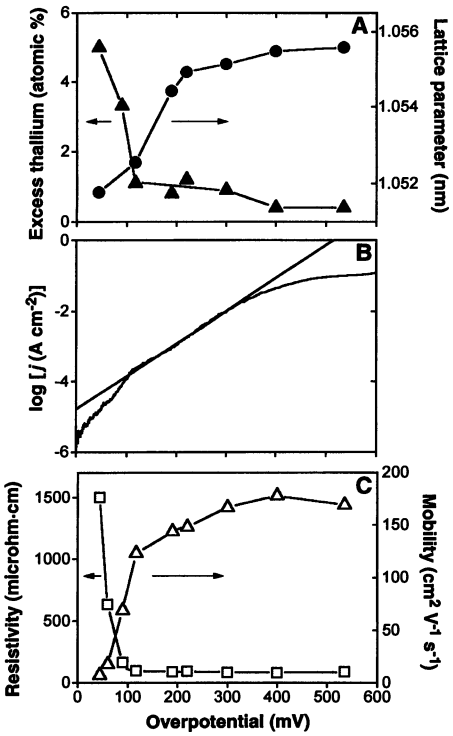

Fig. 3. (**A**) Comparison of the structural properties [(●) lattice parameter and (▲) excess thallium] of bulk thallium(III) oxide films as a function of overpotential. (**B**) The Tafel plot of log j versus overpotential (curve) for the electrodeposition of thallium(III) oxide deviates from linearity. (**C**) Comparison of electronic properties [(□) resistivity and (△) mobility] of bulk films. The structural and electronic properties all change near the overpotential 102 ± 11 mV, at which deviation from linearity occurs in the Tafel plot. We attribute this deviation to the back electron transfer reaction, which produces cation interstitials in the film.

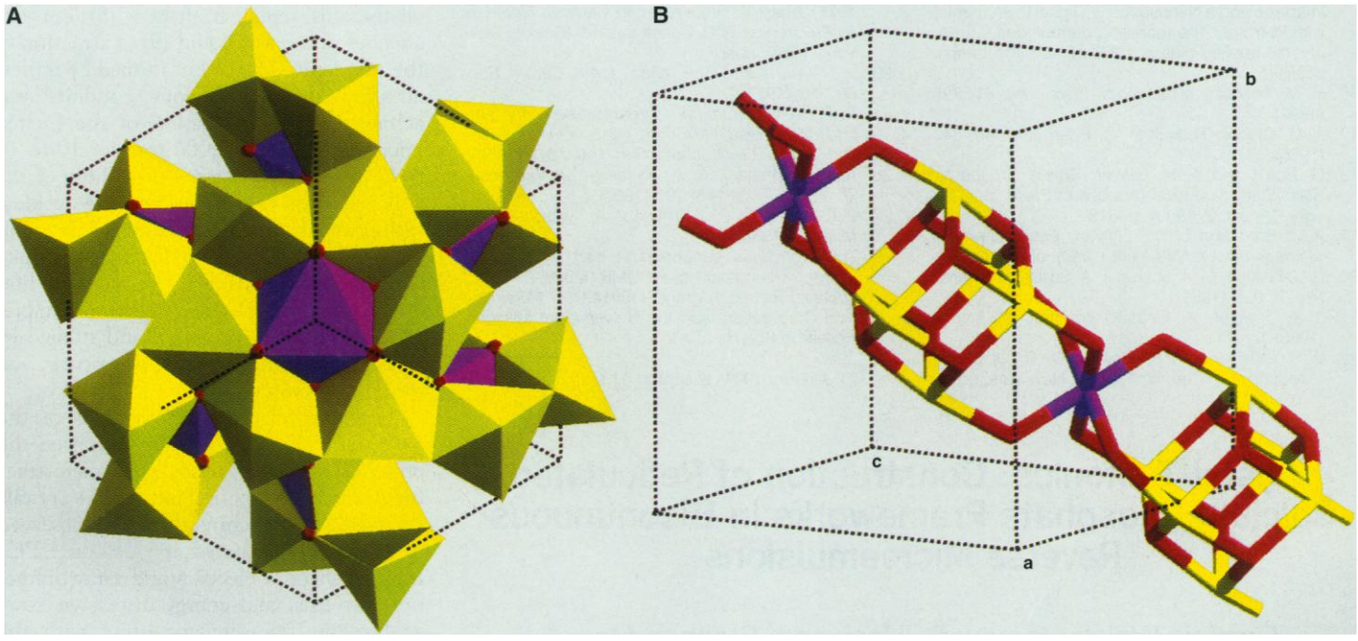

Fig. 4. Crystal structure of thallium(III) oxide. (**A**) Polyhedral model of the structure viewed along the [111] direction. The yellow and purple polyhedra represent two types of thallium coordination environments. The thallium atom in the purple polyhedron at the center of the figure located at ¼, ¼, ¼ and another thallium located at ¾, ¾, ¾ are the end caps of an interstitial hole. There are two of these holes per unit cell. (**B**) Representation that emphasizes the cigar-shaped holes, which lie along the [111] direction and are centered at ½, ½, ½ and 0, 0, 0. The holes have a diameter of 0.33 nm and a length of 0.82 nm. A cation interstitial at the center of each of these holes would be surrounded by six oxygens at a distance of 0.23 nm.

would be more appropriate. The observed carrier density of 5×10^{20} cm^{-3} would require 0.6% of the oxygen sites to be vacant.

This interpretation explains why oxides such as thallium(III) oxide and lead(IV) oxide are highly conducting, whereas indium(III) oxide is not conducting unless doped with an altervalent ion such as tin(IV). Thallium(III) and lead(IV) both have reduction potentials that are positive enough to oxidize a coordinated oxide ion, whereas indium(III) is not a powerful oxidant. The carrier density and mobility that we measure for films grown at high overpotential are very similar to those measured by Wirtz (8×10^{20} cm^{-3} and 120 cm^2 V^{-1} s^{-1}, respectively) on single-crystal thallium(III) oxide produced by vapor transport, in which the high free carrier density was attributed to doubly ionized oxygen vacancies (*23*). The excess thallium content at high overpotentials is insufficient to account for the observed high carrier density of 5×10^{20} cm^{-3}.

The electrodeposited films relax to a carrier density of about 5×10^{20} cm^{-3} regardless of the overpotential used to deposit the film, but the charge compensation defect chemistry is strongly potential dependent: Cation interstitials are favored at low overpotentials, and oxygen vacancies are favored at high overpotentials.

Thallium(III) oxide has the bixbyite crystal structure with the *Ia*3 space group (Fig. 4). This rare earth oxide structure has often been described as a distorted fluorite structure with twice the unit cell dimensions and one-quarter of the oxygens missing (*24*). The thallium atom located at ¼, ¼, ¼ (Fig. 4A) and another thallium atom located at ¾, ¾, ¾ are the end caps of an interstitial hole with a diameter of 0.33 nm and a length of 0.82 nm. There are two of these cigar-shaped holes in the structure, which lie along the [111] direction and are centered at ½, ½, ½ and 0, 0, 0 (Fig. 4B). A thallium interstitial ion located at the center of these holes would be surrounded by six oxygen atoms at a distance of 0.23 nm. If both holes of the structure were filled with thallium interstitials, the excess thallium content would be 6.2%. Hence, the thallium(III) oxide structure is open enough to tolerate rather large interstitial ions or molecules; but the interstices are not interconnected, so the electrochemically imposed defect chemistry can remain localized in these nanometer-scale structures.

The deposition technique we have outlined for defect chemistry superlattices should be applicable to a wide range of electrodeposited compound materials. Examples include PbO_2 (*25*), Cu_2O (*26*), $Ag(Ag_3O_4)_2NO_3$ (*27*), and the electrodeposited superconductor $Ba_{1-x}K_xBiO_3$ (*4*–*7*). The main requirements are an element with variable oxidation states that can be electrochemically controlled and relatively sluggish (that is, Tafel-like) electron-transfer kinetics.

REFERENCES AND NOTES

1. J.-M. Triscone, M. G. Karkut, L. Antognazza, O. Brunner, O. Fischer, *Phys. Rev. Lett.* **63**, 1016 (1989).
2. Z. Fisk and G. Aeppli, *Science* **260**, 38 (1993); R. J. Cava, *ibid.* **247**, 656 (1990).
3. M. Laguës *et al.*, *ibid.* **262**, 1850 (1993).
4. M. L. Norton and H. Y. Tang, *Chem. Mater.* **3**, 431 (1991).
5. G. L. Roberts, S. M. Kauzlarich, R. S. Glass, J. C. Estill, *ibid.* **5**, 1645 (1993).
6. J. M. Rosamilia, S. H. Glarum, R. J. Cava, B. Batlogg, B. Miller, *Phys. C* **182**, 285 (1991).
7. W. D. Mosley *et al.*, *J. Cryst. Growth* **128**, 804 (1993).
8. J.-C. Grenier *et al.*, *Phys. C* **173**, 139 (1991).
9. A. Demourgues *et al.*, *J. Solid State Chem.* **105**, 458 (1993).
10. J. F. DiCarlo, I. Yazdi, S. Bhaverju, A. J. Jacobson, *Chem. Mater.* **5**, 1692 (1993).
11. J. A. Switzer, M. J. Shane, R. J. Phillips, *Science* **247**, 444 (1990).
12. J. A. Switzer and T. D. Golden, *Adv. Mater.* **5**, 474 (1993).
13. J. A. Switzer, R. P. Raffaelle, R. J. Phillips, C.-J. Hung, T. D. Golden, *Science* **258**, 1918 (1992).
14. T. D. Golden, R. P. Raffaelle, J. A. Switzer, *Appl. Phys. Lett.* **63**, 1501 (1993).
15. The superlattices were deposited from an aqueous solution of 100 mM $TlNO_3$ in 1 M NaOH (caution: thallium compounds are extremely toxic). A platinum wire coated with thallium(III) oxide with a potential of −204 mV versus the saturated calomel electrode served as the reference electrode. The substrate was a 3.8-cm^2 stainless steel disc rotated at 500 revolutions per minute. Potentials were controlled with a potentiostat-galvanostat (EG&G Model 273A). We obtained STM

images using a Nanoscope II (Digital Instruments) with Pt-Ir tips. The tunneling current was 0.5 nA, and the applied bias was 200 mV with the sample positive.
16. R. M. Feenstra *et al.*, *Appl. Phys. Lett.* **61**, 795 (1992).
17. J. M. Gibson, R. Hull, J. C. Bean, *ibid.* **46**, 649 (1985).
18. G. Burns and A. M. Glazer, *Space Groups for Solid State Scientists* (Academic Press, San Diego, CA, ed. 2, 1990), p. 313.
19. A. J. Bard and L. R. Faulkner, *Electrochemical Methods* (Wiley, New York, 1980), chap. 3.
20. R. J. Phillips, M. J. Shane, J. A. Switzer, *J. Mater. Res.* **4**, 923 (1989).
21. J. A. Switzer, *J. Electrochem. Soc.* **133**, 722 (1986).
22. W. D. Kingery, H. K. Bowen, D. R. Uhlmann, *Introduction to Ceramics* (Wiley, New York, ed. 2, 1976), chap. 4; H. L. Tuller, in *Ceramic Materials for Electronics*, R. C. Buchanan, Ed. (Dekker, New York, 1986), chap. 8.
23. V. N. Shukla and G. P. Wirtz, *J. Am. Ceram. Soc.* **60**, 253 (1977).
24. A. F. Wells, *Structural Inorganic Chemistry* (Oxford Univ. Press, New York, ed. 5, 1991), p. 545.
25. W. Mindt, *J. Electrochem. Soc.* **116**, 1076 (1969).
26. A. E. Rakhshani, A. A. Al-Jassar, J. Varghese, *Thin Solid Films* **148**, 191 (1987).
27. B. E. Breyfogle, R. J. Phillips, J. A. Switzer, *Chem. Mater.* **4**, 1356 (1992).
28. This work was supported in part by National Science Foundation grant DMR-9202872, Office of Naval Research grant N00014-91-J-1499, Unocal Corporation, and the University of Missouri Research Board.

21 January 1994; accepted 31 March 1994

Crystal Tectonics: Construction of Reticulated Calcium Phosphate Frameworks in Bicontinuous Reverse Microemulsions

Dominic Walsh, Jeremy D. Hopwood, Stephen Mann*

The chemical construction of organized architectures is an important aspect of innovative materials synthesis. Bicontinuous water-filled microemulsions can be used as preorganized systems for the fabrication of crystalline calcium phosphate materials with extended reticulated microstructures. These macroporous materials are formed by mineralization reactions located within the interconnecting water channels of the bicontinuous network. The resulting materials represent replicas of the microemulsion architecture, but the pore sizes are incommensurate, suggesting that secondary modifications in the bicontinuous microstructure occur during crystal growth. Synthetic macroporous calcium phosphates could have uses in biomaterial implants.

Although the elucidation of "molecular tectonics" (*1*) is still at a fundamental level, it is clear that there are many parallels between the synthetic requirements of materials chemistry and the biological strategies inherent in biomineralization (*2*). Previously, we have shown that organized assemblies of amphiphilic molecules can be used to provide nanoscale environments for inorganic materials synthesis, anisotropic templates for the production of fibrous inorganic-organic composites, and recognition surfaces for the oriented nucleation of inorganic crystals (*3*). Although this approach has been successful in mimicking aspects of biomineralization involving discrete building units, it has not been forthcoming in fabricating elaborate three-dimensional extended architectures analogous to the tests and shells of biological materials such as diatoms and sea urchins. The technological importance of such a relation is exemplified in the recent discovery involving the use of liquid-crystal surfactant aggregates in the control of the pore size of amorphous aluminosilicate materials formed from aqueous solution (*4*). Here, we report an approach based on "crystal tectonics," in which the nanoscale interconnecting rod-like water conduits of bicontinuous water-filled microemulsions act as an organized medium for the construction of an extended macroporous calcium phosphate material. Our approach differs from previous studies with liquid-crystal aggregates in that aqueous compartments are used and reticulated frameworks comprising crystalline inorganic units are fabricated. Moreover, because the bicontinuous network microstructure rapidly fluctuates in liquid media, we have used frozen oils to generate immobilized frameworks for the construction of inorganic architectures.

Bicontinuous reverse microemulsions (*5*) were prepared from mixtures of the cationic surfactant didodecyldimethyl ammonium bromide (DDAB), a metastable calcium phosphate aqueous solution, and a long chain alkane (*6*). The clear mixture was rapidly frozen in liquid nitrogen (*7*) and stored for up to several weeks at temperatures (−25°C for dodecane, +2°C for tetradecane, and −25°C or +2°C for tetradecane-hexadecane mixtures) at which the alkane oils remained frozen (*8*) but the aqueous phase was liquid (*9*). Extraction of the inorganic component formed by mineralization in the aqueous conduits was achieved by centrifugation of the melted microemulsion at 10,000 rpm for 10 to 15 min, followed by extensive washing of the pellet in hot hexane to remove residual surfactant and oil. Depending on the volumes of metastable calcium phosphate used, product yields of 0.5 to 1.0 g per liter of microemulsion were obtained. Samples were subsequently air-dried and studied by x-ray diffraction, infrared spectroscopy, and electron microscopy (*10*).

Scanning electron micrographs of the extracted mineralized replicas showed the presence of highly reticulated microstructures of interconnecting needle-like crystals (Fig. 1). These architectures were observed in all samples prepared at −25° or +2°C. Infrared spectra, electron and x-ray diffraction patterns, and energy dispersive x-ray analysis spectra were consistent with the crystalline mineral hydroxyapatite [HAP: $Ca_{10}(OH)_2(PO_4)_6$]. The majority of materials studied were macroporous with pore diameters up to several micrometers and wall thicknesses of 50 to 130 nm, depending on the storage time and composition of the microemulsion mixture (Table 1). No evidence of regular interconnecting arrays was observed; in all structures the framework appeared to consist of a randomly arranged network of intergrown crystalline needles (lengths of 0.2 to 1 μm) with a wide range of pore diameters. The largest pores were often formed by curved cylinders of the reticulated material and were possibly artifacts of the washing and drying processes. Some modifications in microstruc-

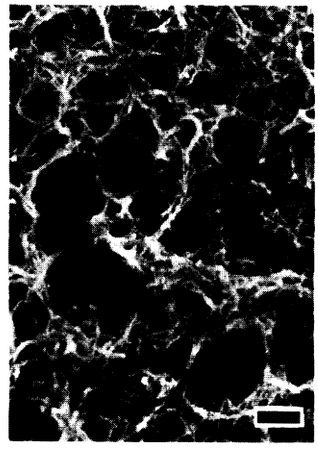

Fig. 1. Scanning electron micrograph showing reticulated framework of needle-like hydroxyapatite crystals formed in bicontinuous microemulsions. The material was prepared from a DDAB-water-tetradecane-hexadecane system at +2°C for 3 weeks. Scale bar, 1.0 μm.

School of Chemistry, University of Bath, Bath, BA2 7AY, UK.

*To whom correspondence should be addressed.